A cobalt-vacant Co_3O_4 as a stable catalyst for room-temperature decomposition of ozone in humid air

Huinan Li [a], Pengyi Zhang [a,b,*], Jingbo Jia [c], Xianjie Wang [a,d], Shaopeng Rong [e]

[a] *State Key Joint Laboratory of Environment Simulation and Pollution Control, School of Environment, Tsinghua University, Beijing 100084, China*
[b] *Beijing Key Laboratory for Indoor Air Quality Evaluation and Control, Beijing 100084, China*
[c] *Beijing University of Chemical Technology, Beijing 100029, China*
[d] *Midea Corporate Research Center, Foshan 528311, China*
[e] *School of Environmental and Biological Engineering, Nanjing University of Science and Technology, Nanjing 210094, China*

ARTICLE INFO

Keywords:
Cobalt oxide
Metal vacancy
Ozone decomposition
Coordination-unsaturated oxygen
Water vapor

ABSTRACT

Conventionally ozone-decomposition catalysts such as MnO_2 face the gradual deactivation due to occupation of reactive site, i.e., oxygen vacancy by intermediates like O_2^{2-} or ubiquitous water vapor in air. Herein, we synthesized a Co^{2+}-vacant Co_3O_4 ($Co_{3-x}O_4$) with dominant exposure of (110) facets, it maintained superior efficiency of 98% in decomposing 100 ppm ozone over 180 h under the space velocity of 1200 L/g·h at 25 ℃ and relative humidity (RH) of 50%, well beyond the performance of any reported metal oxides catalysts. Especially, it kept stable efficiency even under RH 90% and ultrahigh space velocity of 6000 L/g·h. A new ozone decomposition mechanism under humid conditions is revealed, i.e., the Co^{2+} vacancy significantly promotes O_3 adsorption and the hydroxylation of coordination-unsaturated oxygen (CUO), and Co^{3+} work together with surface OH group to decompose ozone avoiding the deactivation. This study demonstrates a new way, i.e., creating metal vacancy rather than oxygen vacancy to design stable and efficient catalysts for ozone decomposition under humid conditions.

1. Introduction

Ozone is one of the classical air pollutants regulated by World Health Organization [1] and is subject to regulations in many countries. People in daily life are inevitably exposed to ozone. It comes not only from outdoors generated from photochemical reaction between nitrogen oxides (NOx) and volatile organic compounds (VOCs) [2], but also from various household electric equipment such as photocopiers, laser printers, sterilizing devices and air purifiers [3]. In recent years, the universal pollution of ground level ozone has increasingly attracted worldwide attention owing to its damage to human health [4–6]. Due to its strong oxidation and high reactivity, exposure to either long-term or short-term ozone has been linked to an increased morbidity such as respiratory [7], cardiovascular [5] and cardiopulmonary diseases [8], as well as serious adverse pregnancy outcomes [9]. Besides direct hazard, various ozone reactions especially in indoor environment would induce a series of secondary pollutants such as organic aerosols, aldehydes and carboxylic acids, which may be more harmful to human health than

ozone itself [10]. Thus, it is of great importance to eliminate ozone pollution for environment protection and human health.

Room-temperature catalytic decomposition has attracted extensive attention as it dissociates O_3 into O_2 without producing harmful byproducts and consuming any extra energy [11–15]. A lot of catalysts have been investigated for ozone dissociation such as noble metal like Ag [16], Pd [17], Au [18] and Ru [19] and transition metal oxides (TOMs) like MnO_x [20], NiO [21], Fe_2O_3 [22], CuO [23], Co_3O_4 [24], CeO_2 [11], and so forth. Among TOMs, MnO_2 appears to be the most promising catalyst with higher efficiency and earth abundance [11,20], thus it has been widely studied. However, its gradual deactivation under humid condition still needs to be solved.

It is well recognized that oxygen vacancies in TMOs act as reaction sites for the ozone decomposition [12,25,26], and the desorption of relative stable intermediates, i.e. peroxide (O_2^{2-}) limits the speed of the catalytic cycle in most cases [27]. Due to its small local work function, oxygen vacancy cannot soon capture electron from peroxide (O_2^{2-}) to recover the active site, consequently resulting in a depressed

ozone-decomposition efficiency [28]. Besides, water molecules ubiquitously in air usually occupy the oxygen vacancies and hinder the adsorption of ozone molecule. The competitive adsorption of water molecules on the oxygen-vacancy sites and subsequent dissociation, which might occupy the oxygen vacancy permanently, would significantly lower the ozone decomposition efficiency and lead to gradual deactivation especially under the high humid conditions. To improve the performance of catalysts under humid conditions, many efforts have been made. One way is to increase the content of oxygen vacancies, which aims to provide more reaction sites via cation doping [11,29], lattice distortion [30], surface etching [26], interlayer and tunnel ion exchange [25,31]. The other way is to modify the surface property of catalysts to increase their hydrophobicity via heat treatment [32] and coverage with hydrophobic material such as graphene [28]. However, the intrinsic property of oxygen vacancies, i.e., susceptible to water vapor and O_2^{2-} intermediate species does not change, it is highly desired to develop a new strategy to overcome the deactivation problem caused by water occupation and O_2^{2-} accumulation on the oxygen-vacancy sites.

The cation vacancy, another kind of vacancy, is stable and can also acts as adsorption and reaction site. Co_3O_4 receives ever-growing interests in thermal catalytic oxidation of pollutants and electrocatalytic water oxidation. Though Co_3O_4 has been reported to show high activity for CO and volatile organic compounds, it is rarely reported for ozone decomposition. Here, we choose Co_3O_4 to tune its cation vacancy rather than oxygen vacancy to generate active site for ozone decomposition [33,34]. A Co_3O_4 catalyst with abundant cobalt vacancies and dominant exposure of (110) facet was synthesized, which exhibited extraordinarily high and stable activity for ozone decomposition even under high humid and ultrahigh space velocity conditions. We found it decomposes ozone via a new catalytic mechanism much different from the well-known oxygen-vacancy based mechanism.

2. Experimental section

2.1. Catalyst preparation

4.98 g cobalt acetate tetrahydrate and 60 mL ethylene glycol were mixed, which was heated to 160 °C and kept for 1.5 h. After that, 200 mL 0.2 M Na_2CO_3 aqueous solution was added in, and the slurry was further aged until the solution dried. During the whole synthesis process, the mixture was continuously stirred and protected by the flow of nitrogen gas. The final precipitate was filtered and washed with water and ethyl alcohol, then it was dried at 50 °C overnight in a vacuum drying oven, and finally calcined at 450 °C for 4 h in air.

2.2. Catalyst characterization

X-ray diffraction (XRD) patterns were checked by a Bruker X-ray diffractometer (D8-Advance, Germany) with a Cu Kα X-ray source. Morphologies of the samples were observed by a scanning electron microscopy (SEM, Geminisem 500) and a transmission electron microscopy (TEM, JEOL-2011). X-ray photoelectron spectrometer (XPS) analysis was conducted with a Thermo Fisher (Escalab Xi+, USA) equipment and the binding energy was calibrated with the signal for carbon at 284.8 eV. The element compositions of samples were investigated by inductively coupled plasma optical emission spectrometer (ICP-OES, Thermo, IRIS Intrepid II) and total organic carbon analysis (Shimazu, TOC-LCPH).

Positron annihilation lifetime spectra (PALS) were measured using an ORTEC-928 fast-fast coincident system at room temperature. The sample powder was pressed into a disk (diameter: 10.9 mm, thickness: 1.0 mm). A ^{22}Na positron source was sandwiched between two identical sample disks. X-ray absorption near edge structure (XANES) was detected at BL14W beamline in Shanghai Synchrotron Radiation Facility (SSRF). The storage rings of SSRF were operated at 3.5 GeV with a stable current of 200 mA. The incident beam was monochromated by Si (111) double-crystal monochromator. All spectra were collected in ambient

conditions. Data reduction, data analysis, and data fitting were performed with the Athena and Artemis software packages.

In situ Raman spectroscopy was carried out on a Raman microscope (inVia, Britain) and a CCR1000 catalyst cell reactor system (Linkam Scientific Instruments). The catalyst powder ~100 mg was placed in the cell. In situ Raman spectra was continuously acquired under the different gas flow, i.e., O_2, O_3 or O_3/H_2O at room temperature, and under O_2, O_3 flow at different temperatures. The total flow rate was 100 mL·min^{-1}. The inlet ozone concentration was set at ~ 800 ppm.

In-situ diffuse reflectance infrared Fourier transform spectroscopy (DRIFTS) was conducted on a Nicolet 6700 to detect the change of surface OH group. After treated in air flow at 200 °C for 2 h and cooled to room temperature, the samples were subsequently exposed to RH 100% O_2, dry O_2 and dry O_3 flow.

Density functional theory (DFT) calculations were performed using the Vienna ab initio simulation package (VASP) code for surface energy, adsorption energy and transition state and more details are described in the Supporting Information.

2.3. Catalytic activity test

The performance of catalyst for ozone decomposition was evaluated in a quartz tube with the diameter of 6 mm at 25 °C unless otherwise noted. Catalyst powder with size of 40–60 mesh was used. The experiment setup is shown in Fig. S1. The total flow rate was 1 L/min, and the relative humidity (RH) was adjusted by the mass flowmeters. The RH of the gas was measured by a hygrometer (testo 635–2) with an accuracy of 0.1% and the error of which no more than ± 0.5%. The inlet ozone concentration was ~ 100 ppm, which was generated with the oxygen gas flow under the irradiation of a low-pressure mercury ultraviolet lamp. The ozone concentration was analyzed by an online ozone analyzer (Model 49i, Thermo Fisher Scientific, USA) with an accuracy of 1 ppb. The ozone conversion was calculated as follows:

$$\text{Ozone Conversion} = \frac{C_{in} - C_{out}}{C_{in}} \times 100\%$$

where C_{in} and C_{out} represent inlet and outlet ozone concentration, respectively.

3. Results and discussion

3.1. Synthesis and characterization of Co-vacant $Co_{3-x}O_4$

The Co-vacant Co_3O_4, i.e., $Co_{3-x}O_4$ was synthesized by calcining the Co(II)-ethylene glycol (Co-EG) at 450 °C for 4 h. The Co-EG was prepared by heating the mixture of cobalt acetate and ethylene glycol at 160 °C and then purifying with sodium carbonate. As-synthesized Co-EG was weakly crystallized with four weak peaks at ca. 11, 33, 59 and 70° in XRD pattern (Fig. 1A) [35]. The Co-EG has a layered crystal structure consisting of stacked metal-oxygen sheets separated by bonded ethylene glycol anions, which is beneficial to the formation of metal vacancies in oxide crystals during calcination [36]. After calcined at 450 °C for 4 h, the Co-EG was transformed into spinel Co_3O_4 (JCPDS No. 09–0418) without any other crystal phases (Fig. 1B).

SEM images (Fig. 1C) indicated that Co-EG looked like a flower consisting of nanosheets with the length about 200–300 nm. After calcined, as-obtained $Co_{3-x}O_4$ (Fig. 1D) still holds the flower structure, however it can be seen that nanosheets were broken into smaller ones. Due to its flower-like structure, $Co_{3-x}O_4$ had higher specific surface area (136 m^2/g) than the commercial Co_3O_4 (40.3 m^2/g) (Table 1). In transmission electron microscopy (TEM, Fig. 1E) image, many irregular holes (circled in red) formed during the calcination process can be found on $Co_{3-x}O_4$ sheets, which was beneficial to the mass transfer. High-resolution transmission electron microscopy (HRTEM, Fig. 1F and S2) images showed the lattice fringes of 0.28 and 0.24 nm corresponding to the (220) and (311) planes of spinel Co_3O_4. The fast Fourier transform pattern (inset in Fig. 1F) exhibited the angle of 65° identical to the
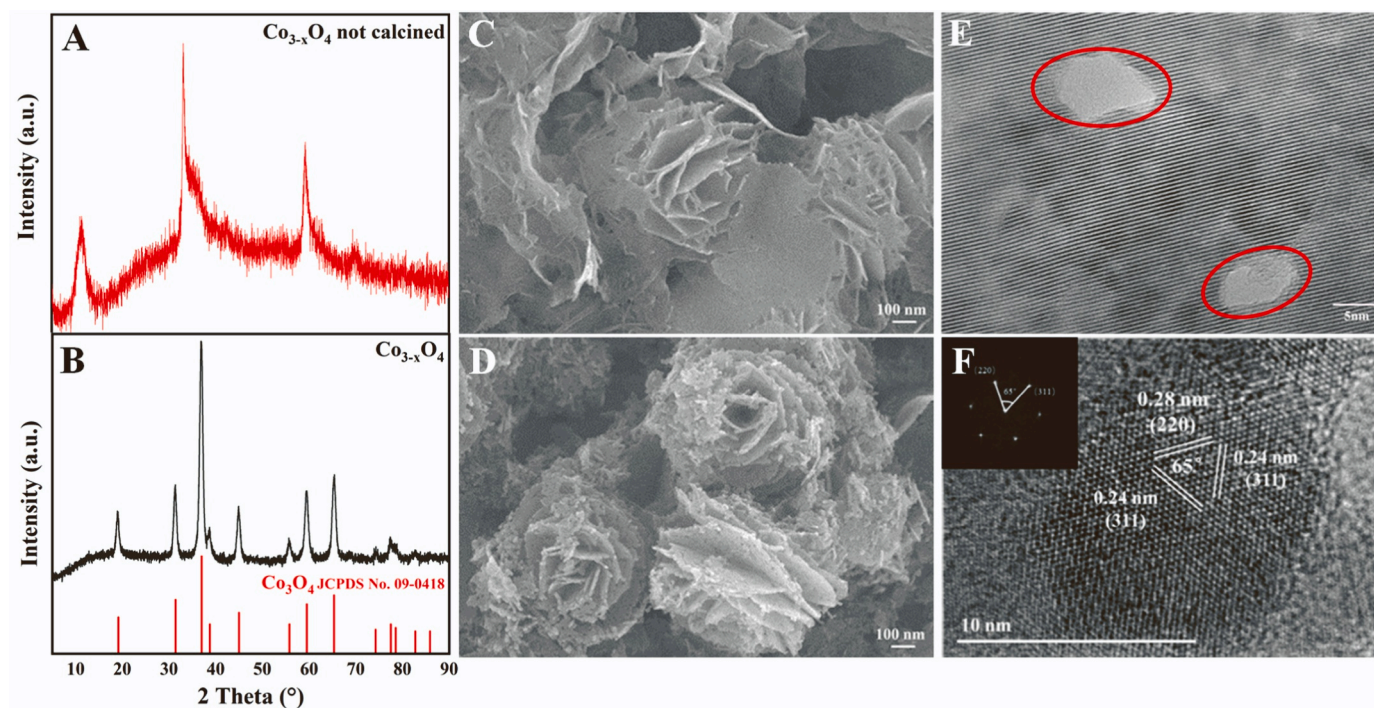
Fig. 1. XRD patterns of (A) $Co_{3-x}O_4$ precursor and (B) $Co_{3-x}O_4$; SEM images of (C) $Co_{3-x}O_4$ precursor and (D) $Co_{3-x}O_4$; (E) TEM image of $Co_{3-x}O_4$; (F) HRTEM image and FFT (inset) of $Co_{3-x}O_4$.

Table 1
Specific surface area, element composition, positron lifetime (τ) and intensity (I) of $Co_{3-x}O_4$ and commercial Co_3O_4.

Samples	Specific surface area (m^2/g)	Atomic ratio of Co/O		τ_1 (ps)	I_1 (%)	τ_2 (ps)	I_2 (%)
		by ICP-OES	by XPS				
$Co_{3-x}O_4$	136	0.619	0.569	208	49.17	424	50.83
Commercial Co_3O_4	40.3	0.712	0.594	166	31.93	365	68.07

theoretical value of the angle between (220) and (311) facets. The above results mean the main exposed facet of $Co_{3-x}O_4$ was (110) facet, which favors the exposure of Co^{3+} atoms on the surface [37]. The absence of (110) facet in XRD pattern of Co_3O_4 is due to the systematic extinction in X-ray diffraction of Co_3O_4 (Fig. S3) [38].

To confirm whether cobalt vacancies had been generated, the commercial Co_3O_4 with high crystallinity was taken as a reference. Though both samples exhibited same spinel phase (Fig. S3), their composition were much different. As shown in Table 1, the molar ratio of Co/O obtained from inductively coupled plasma optical emission spectrometer (ICP-OES) measurement was 0.712 in commercial Co_3O_4, which was close to the stoichiometric ratio of 0.75. However, it was only 0.619 in $Co_{3-x}O_4$, indicating the presence of Co vacancy. X-ray photoelectron spectrometer (XPS) results (Table 1) also showed that $Co_{3-x}O_4$ had lower surface Co/O ratio than that of commercial Co_3O_4.

Metal vacancy in metal oxides is a kind of point defect, which may influence the positron annihilation. Thus, positron annihilation lifetime spectra (PALS) were measured for both samples. As shown in Table 1, both samples exhibit two different lifetime values (τ_1, τ_2), corresponding to two kinds of vacancies with different size. The shorter lifetime (166–208 ps) can be assigned to the annihilation of positrons in the single metal vacancy, while the longer lifetime (365–424 ps) is assigned to the annihilation of vacancy clusters [36]. Either the shorter or the longer lifetime for $Co_{3-x}O_4$ are higher than those of the commercial

Co_3O_4, especially $Co_{3-x}O_4$ had higher τ_1 lifetime and I_1 intensity, which indicated that $Co_{3-x}O_4$ had more abundant single metal vacancy than commercial Co_3O_4.

The X-ray absorption near edge structure (XANES) and extended X-ray adsorption fine structure (EXAFS) were further used to investigate the structure of as-synthesized $Co_{3-x}O_4$. As shown in Fig. 2 A, the shapes of the edges for $Co_{3-x}O_4$ and commercial Co_3O_4 were similar, while a comparison of the inflection points obtained from the second derivative plots indicated that the edge of $Co_{3-x}O_4$ was 0.32 eV higher than that of commercial Co_3O_4 (inset in Fig. 2 A). This result indicates that $Co_{3-x}O_4$ possessed a relatively higher Co oxidation state, which is consistent with its lower ratio of Co/O shown in Table 1. In addition, R space was obtained by Fourier transformation from wavevector k (Fig. 2B). Both samples showed four prominent peaks mainly caused by the single scattering of Co-O, Co-Co$_1$, Co-Co$_2$ and Co-Co$_3$, respectively. The amplitude of R space is positively correlated with coordination number and negatively correlated with mean-square disorder, and vice versa. From the peaks of Co-Co$_1$, Co-Co$_2$ and Co-Co$_3$, it is obvious that $Co_{3-x}O_4$ had lower Co-Co coordination number and higher mean-square disorder, indicating the presence of many Co vacancies in $Co_{3-x}O_4$ structure. The first three mean peaks were fitted and the results are shown in Table 2. The coordination numbers for bonding Co with Co atoms in different distance shells of $Co_{3-x}O_4$ were less than those of the commercial Co_3O_4, which led to an increase in mean-square disorder. Thus, according to the above analysis, we can conclude that more Co vacancies (V_{Co}) exist in the $Co_{3-x}O_4$ structure [39,40].

In order to study the effect of metal vacancy on electronic structure, the density functional theory (DFT) calculations were conducted. As we know, in the structure of Co_3O_4, cobalt ions exist in the form of either Co^{3+} or Co^{2+}. Thus, it is interesting to know which kind of cobalt ions are preferentially absent in $Co_{3-x}O_4$. The calculation result indicates that the formation energy of Co^{2+} vacancy (1.09 eV) is lower than that of Co^{3+} vacancy (1.64 eV), suggesting that Co^{2+} vacancies are easier to be formed and are the major Co vacancies in $Co_{3-x}O_4$. In addition, the partial charge density is calculated and shown in Fig. S4, in comparison with normal Co_3O_4, the Co vacancies result in distortion of neighboring

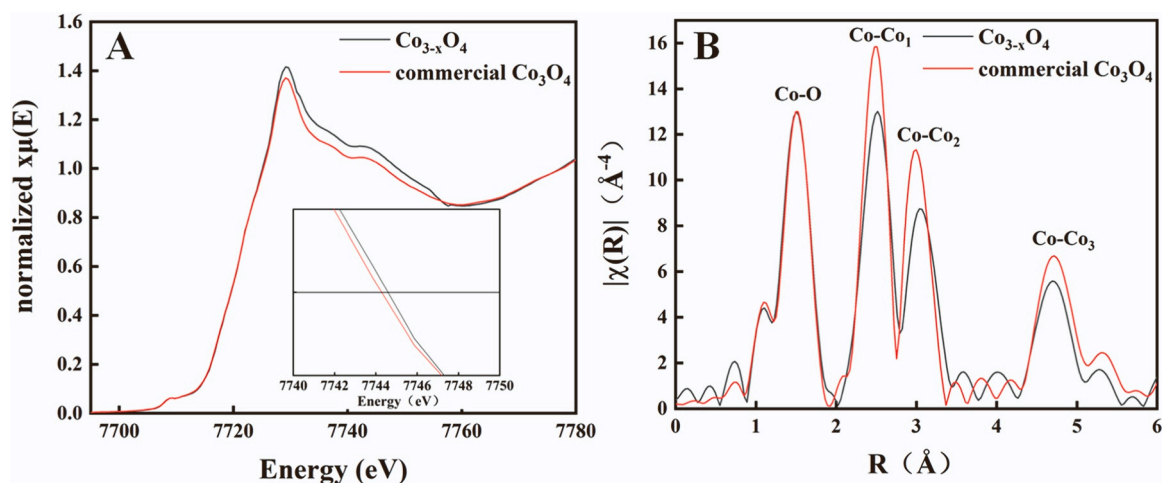**Fig. 2.** (A) XANES and second derivative plots (inset), and (B) Fourier transforms of *k*-space oscillations for $Co_{3-x}O_4$ and commercial Co_3O_4.

Table 2
Fitted parameters of Co K-edge EXAFS curves for $Co_{3-x}O_4$ and commercial Co_3O_4.

Sample	Path	Coordination number	Debye-Waller factor σ^2 (Å^{-2})	Amplitude attenuation factor S_0^2
$Co_{3-x}O_4$	Co-O	5.7 ± 0.3	0.0020 ± 0.0006	0.686
	Co-Co_1	4.3 ± 0.8	0.0053 ± 0.0013	
	Co-Co_2	6.2 ± 1.4	0.0065 ± 0.0016	
Commercial Co_3O_4	Co-O	5.8 ± 0.5	0.0021 ± 0.0009	0.686
	Co-Co_1	5.1 ± 1.3	0.0038 ± 0.0016	
	Co-Co_2	9.6 ± 2.5	0.0063 ± 0.0018	

atoms and obvious electronic delocalization, which is confirmed by XPS results. As shown in Fig. S5, the binding energy values of O 1 s and Co 2p on the surface of $Co_{3-x}O_4$ are all slightly smaller than those of commercial Co_3O_4, implying the corresponding electronics are more easily excited by X-ray. H_2-TPR results (Fig. S6) showed that the both reduction peaks of $Co_{3-x}O_4$ occurred at much lower temperatures than those of commercial Co_3O_4, which further confirmed the active species on the surface of $Co_{3-x}O_4$ were more active.

3.2. Catalytic performance of $Co_{3-x}O_4$ for ozone decomposition

The catalytic activity of $Co_{3-x}O_4$ for O_3 decomposition was evaluated at room temperature in a fixed-bed reactor at the inlet O_3 concentration of 100 ppm. It is highly desirable to develop catalysts with superior activity and durability under the high humid conditions. Here, we first tested its performance under various weight hour space velocities (WHSV) by adjusting the amount of $Co_{3-x}O_4$ sample in the reactor, i.e., 10, 20 30, 40, 50 mg and keeping the flow rate constant at 1 L/min, corresponding to the WHSV of 6000, 3000, 2000, 1500 and 1200 L/g·h respectively. And the relative humidity was kept constant at 50%. As shown in Fig. 3A, under all these different space velocities, $Co_{3-x}O_4$ kept stable activity during the every 500-min test. Especially, even under the ultrahigh WHSV of 6000 L/g·h, the performance of $Co_{3-x}O_4$ did not decrease a little. The ozone removal efficiency decreased with the increase of space velocity, from ~99% at WHSV of 1200 L/g·h to ~49% at WHSV of 6000 L/g·h, and the ozone decomposition rate obeyed the first-order kinetics with the reaction rate constant of 276.3 s^{-1} (Fig. S7).

Furthermore, we checked the performance of $Co_{3-x}O_4$ under different relative humidity from the dry condition to RH 90%. It is noteworthy that the normal dry air or nitrogen gas contains trace water vapor about 3.1 ppm detected by a dew-point hygrometer (DMT141-DP). As shown in Fig. 3B, under the WHSV of 1200 L/g·h the ozone-decomposition efficiency of $Co_{3-x}O_4$ was little influenced when the RH was no more than 50%, almost keeping > 99%. When the RH increased to 75% and 90%, the ozone removal efficiency decreased to 86% and 80%, respectively, indicating the effect of water competitive occupation on the reaction sites. However, the removal efficiency became very stable within 500 min after initial short balance stage. The durability of $Co_{3-x}O_4$ in a longer time was also checked under WHSV of 1200 L/g·h and RH 50%, it kept stable efficiency as high as 98% in the 180 h test (Fig. 3C), while the commercial Co_3O_4 soon lost its activity within 5 min (inset in Fig. 3C) to less than 10%, suggesting the significance of the special $Co_{3-x}O_4$ structure on its ozone-decomposition activity. These results clearly indicate that $Co_{3-x}O_4$ can not only resist the deactivation caused by the accumulation of intermediate products, but also greatly inhibit the adverse impact of water vapor.

The activity of $Co_{3-x}O_4$ at different air temperature was also checked. Like the effect of relative humidity, $Co_{3-x}O_4$ activity was little influenced even when the air temperature was as low as 0 ℃, keeping nearly 100% ozone removal efficiency (Fig. 3D). When the temperature further decreased to − 10 ℃, within 2 h the ozone removal efficiency decreased to 97%. Compared with other ozone-decomposition catalysts including traditional metal oxides, LDH and MOFs (Table S1), $Co_{3-x}O_4$ exhibits obvious advantages in activity and stability at room temperature and in common humidity. In addition, it also exhibited high activity at temperature as low as − 10 ℃, which indicates $Co_{3-x}O_4$ not only has promising application for room-temperature but also for low-temperature conditions such as for treating ozone-containing air entering airplane cabinet at high altitude, where the air temperature is very low [41].

3.3. Discussion on the ozone decomposition mechanism

3.3.1. The reaction sites for ozone decomposition over $Co_{3-x}O_4$

Oxygen vacancies are well recognized as the reaction sites for ozone decomposition over most metal oxides [20,27,29,42], and in most cases the desorption of peroxide specie (O_2^{2-}) from the oxygen vacancy site is regarded as the rate-limiting step. To know whether oxygen vacancy also is the reaction site of $Co_{3-x}O_4$ for ozone decomposition, we first used Raman spectrometer to check peroxide species on the surface of $Co_{3-x}O_4$ during ozone decomposition in various conditions. As mentioned above, ozone decomposition efficiency decreased under high RH and at low temperatures, thus under these conditions intermediates
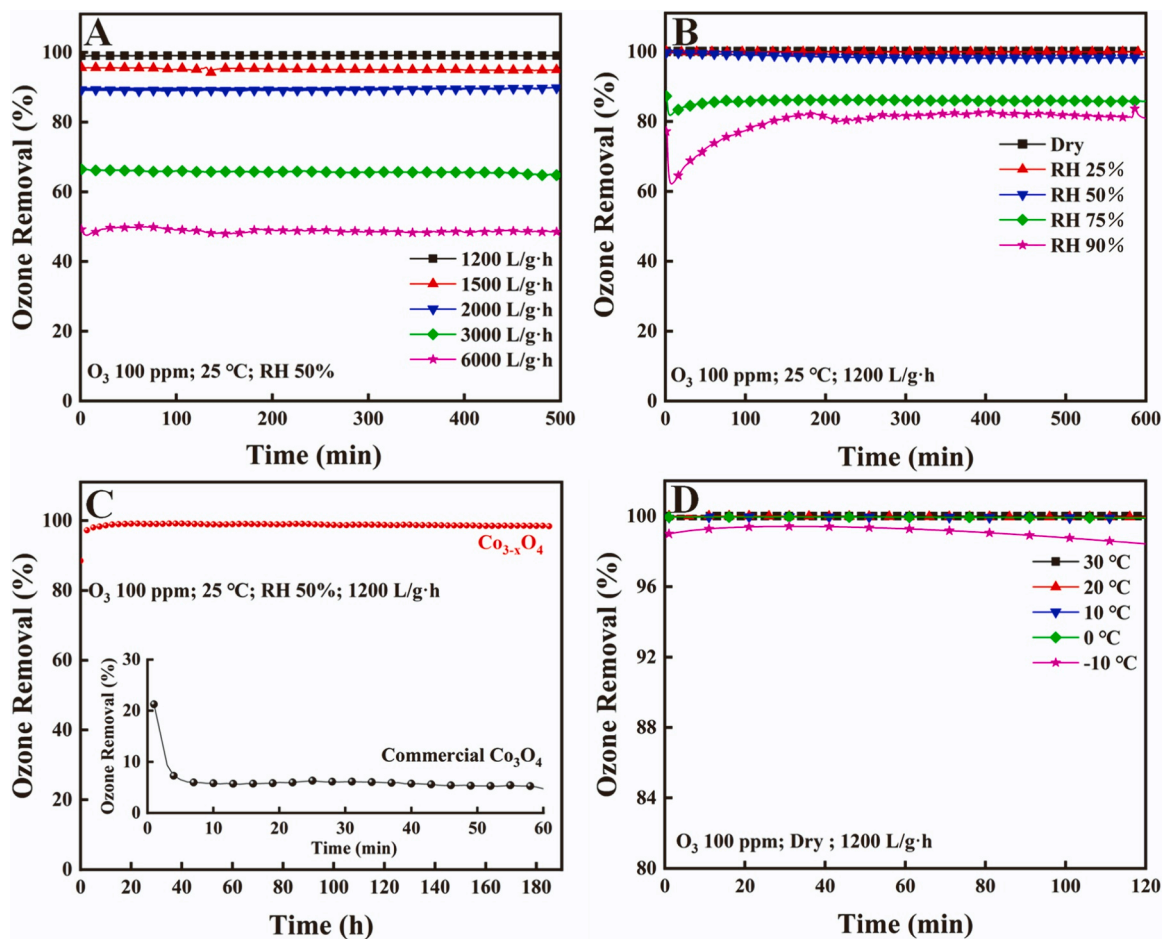
Fig. 3. Ozone decomposition efficiency over $Co_{3-x}O_4$ under different conditions. (A) under different weight hour space velocity; (B) under different relative humidity; (C) in a long test time with the inset of commercial Co_3O_4 performance; (D) under different reaction temperature.

such as peroxide species are more likely accumulated. However, as shown in Fig. S8, whether under dry or RH 90% condition (Fig. S8A), and under dry condition at different temperature from 25 °C to − 65 °C (Fig. S8B), there was no characteristic signal of peroxide species occurred in the region of 800–900 cm^{-1} (pink shadow in Fig. S8). While the obvious peroxide species were detected during dry and RH 100% ozone decomposition over MnO_2 (Fig. S9) [20], which is a well-known oxygen-vacancy based catalyst. The above results indicate ozone decomposition over $Co_{3-x}O_4$ is different from the oxygen-vacancy pathway and the oxygen vacancy may not the reaction sites for ozone decomposition. And as stated above, it is the cation (Co^{2+}) vacancy not the oxygen vacancy that exist in $Co_{3-x}O_4$ structure. Thus, we think a new mechanism rather than oxygen vacancy mechanism that dominates the ozone decomposition over Co-vacant $Co_{3-x}O_4$.

In the crystal structure of Co_3O_4, normally Co^{2+} is at the tetrahedron site and Co^{3+} is at the octahedron site. The outer electron orbital of Co^{3+} ($3d^5 4s^1$) has an unpaired electron, while Co^{2+} has the full-occupied 4 s orbital ($3d^5 4s^2$), which makes Co^{3+} easier to be adsorbed by ozone than Co^{2+}. Thus, as the first step of ozone decomposition over $Co_{3-x}O_4$, ozone is more likely to be adsorbed on Co^{3+} site, and Co^{3+} acts as the reaction site for ozone decomposition. DFT calculations were performed to verify the rationality of Co^{3+} as ozone adsorption site. As shown in Fig. 4, a clean (110) plane with a Co^{2+}-vacancy model (Co^{2+}-110) was optimized, and the adsorption energies of O_3 on the Co^{3+}, Co^{2+} and coordination-unsaturated O site were calculated, which are − 1.84, − 1.03 and − 0.79 eV, respectively. The more negative adsorption energy, the stronger adsorption is. Thus, O_3 is most likely adsorbed to Co^{3+} site among investigated three sites. Moreover, the adsorption energy of

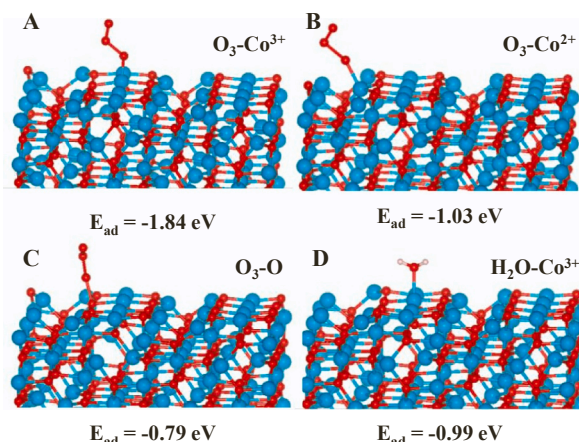**Fig. 4.** Adsorption energy of O_3 on (A) Co^{3+} site, (B) Co^{2+} site, and (C) coordination-unsaturated O of Co^{2+}-vacant (110) plane of Co_3O_4; (D) adsorption energy of H_2O on Co^{3+} site of Co^{2+}-vacant (110) plane.

O_3 on Co^{3+} of Co^{2+}-vacant (110) plane is obviously more negative than that on the perfect (110) plane (Fig. S10), indicating that the Co^{2+} vacancy can significantly enhance ozone adsorption to Co^{3+} site and accordingly increase the ozone decomposition efficiency. Furthermore, we investigated the effect of surface Co^{3+} content on the ozone decomposition efficiency. We used XPS to measure the cobalt valence state of fresh $Co_{3-x}O_4$, used $Co_{3-x}O_4$ (after long-time exposure to high

ozone its ozone decomposition efficiency decreased about 20% in comparison with fresh $Co_{3-x}O_4$), and commercial Co_3O_4. As shown in Fig. S11, the corresponding Co^{2+}/Co^{3+} ratios were 0.374, 0.423 and 0.506, indicating the relative Co^{3+} content is positively correlated with the ozone decomposition efficiency of catalysts. All these results imply Co^{3+} may be the reaction site for ozone decomposition.

3.3.2. The effect of water vapor and surface hydroxylation on ozone decomposition

As mentioned above (Fig. 3B), the ozone decomposition efficiency of $Co_{3-x}O_4$ did decrease with the increase of relative humidity, confirming the adverse impact of water adsorption. However, compared with other catalysts, $Co_{3-x}O_4$ still exhibits much higher activity and longer durability under high humid conditions. As we know, water molecules may occupy the reaction sites via non-dissociative or dissociative adsorption on the surface of metal oxide catalysts, which generally deteriorates the catalytic performance as reported before [12,28,30,31]. To fundamentally learn the effect of water on ozone decomposition, the adsorption energies of H_2O ($E_{ads}^{H_2O}$) on Co^{3+} site of Co^{2+}-vacant (110) plane was also calculated, which is -0.99 eV (Fig. 4D). This result indicates that water would spontaneously adsorb on Co^{3+} site though O_3 is more easily adsorbed ($E_{ads}^{O_3} = -1.84eV$). Because the absolute concentration of water in air is generally two orders higher than ozone concentration, for example RH 75% at 25 ℃ corresponding to water vapor of 23460 ppm, it is understandable that the catalytic performance of $Co_{3-x}O_4$ was decreased under high humid conditions. However, the adsorption energy difference between O_3 and H_2O on Co^{2+}-vacant $Co_{3-x}O_4$ is as high as, i.e., $E_{ads}^{O_3} - E_{ads}^{H_2O} = -0.85eV$. As reported before [20], NH_4^+-modulated ultrathin δ-MnO_2 nanosheet showed superior activity for gaseous ozone decomposition under humid conditions, and the corresponding adsorption energy difference between O_3 and H_2O was -0.66 eV, indicating $Co_{3-x}O_4$ may be more resistant to water vapor. Actually, the ozone decomposition performance confirms the calculation results, $Co_{3-x}O_4$ exhibits better activity than NH_4^+-modulated ultrathin δ-MnO_2 under high humidity.

In addition to the adverse impact of water vapor, we observed a new phenomenon, which indicates the necessity of water vapor for keeping stable activity of $Co_{3-x}O_4$. As shown in Fig. 3B, in the case of high humid conditions (RH 75% and 90%), the ozone decomposition efficiency in the initial time obviously increased with the test time and then reached a stable state. We suppose the quick non-dissociative adsorption of water greatly inhibits the ozone decomposition, while the subsequent dissociation of water, i.e., surface hydroxylation is necessary for ozone decomposition. To verify this hypothesis, we first investigated the

ozone-decomposition efficiency of $Co_{3-x}O_4$ in dry condition (water vapor was only 3.1 ppm) under ultrahigh space velocity (6000 L g_{cat}^{-1} h^{-1}). As shown in Fig. 5 A, under this condition, the ozone decomposition efficiency of $Co_{3-x}O_4$ gradually fell from 95% to 91% within 2 h. Then the dry ozone flow was turned off, and the $Co_{3-x}O_4$ sample was flowed with RH 50% O_2 gas for 2.5 h. After that, the dry ozone again flowed through the water vapor-treated $Co_{3-x}O_4$ sample. We can see in Fig. 5 A that the ozone decomposition efficiency recovered to 96% and then again gradually decreased but only to 94% within 9 h, while it did not decrease under RH 50% (Fig. 3A). The above result implies that ozone decomposition over $Co_{3-x}O_4$ needs to consume adsorbed water or surface hydroxyl group.

Furthermore, we used in-situ DRFITS to check the change of surface functional groups during ozone decomposition. The $Co_{3-x}O_4$ was first pretreated with RH 100% O_2 for 1 h, and then changed to dry O_2 flow for 1 h to wipe off the most adsorbed H_2O molecules, and the $Co_{3-x}O_4$ in this state was taken as the baseline. Subsequently, dry O_2 further flowed for 1 h, and then followed by 10000 ppm dry O_3 for 30 min. The change of in-situ DRFIT spectra is shown in Fig. S12B, and Fig. 5B shows the enlarged area around 1350 cm^{-1}. After treated by dry O_2 for 1 h, the peak 1350 cm^{-1} corresponding to the hydroxyl groups [43] decreased a little. However, when further treated with dry O_3 for only 1 min, the hydroxy group peak greatly decreased and continuously decreased with ozone exposure time, confirming the consumption of hydroxyl groups during ozone decomposition. In conclusion, the above results indicate that there are surface hydroxyl groups consumption during the process of ozone decomposition over $Co_{3-x}O_4$ and they are necessary for keeping stable ozone decomposition activity.

The subsequent interesting question is whether the Co^{2+} vacancy stimulates the surface hydroxylation. We calculated the Gibbs free energy of hydroxylation on the perfect (110) plane and on the Co^{2+}-vacant (110) plane. As shown in Fig. 6A, the Gibbs free energy on the perfect (110) plane is as high as 0.68 eV, while it is -0.13 eV to turn coordination-unsaturated oxygen atom into hydroxyl group (Fig. 6B). The above calculation results indicate the existence of Co^{2+} vacancy greatly stimulates the surface hydroxylation. In other words, the coordination-unsaturated oxygen atoms which are concurrent with Co^{2+} vacancies could spontaneously turn into hydroxyl group in the presence of water vapor.

3.3.3. Ozone decomposition pathway over $Co_{3-x}O_4$

In the above two subsections, we illustrated that Co^{3+} might be the reaction site and Co^{2+}-vacancy induced hydroxylation is necessary for keeping stable activity of $Co_{3-x}O_4$. The subsequent question is how Co^{3+} and surface OH group work together to decompose ozone, i.e., the
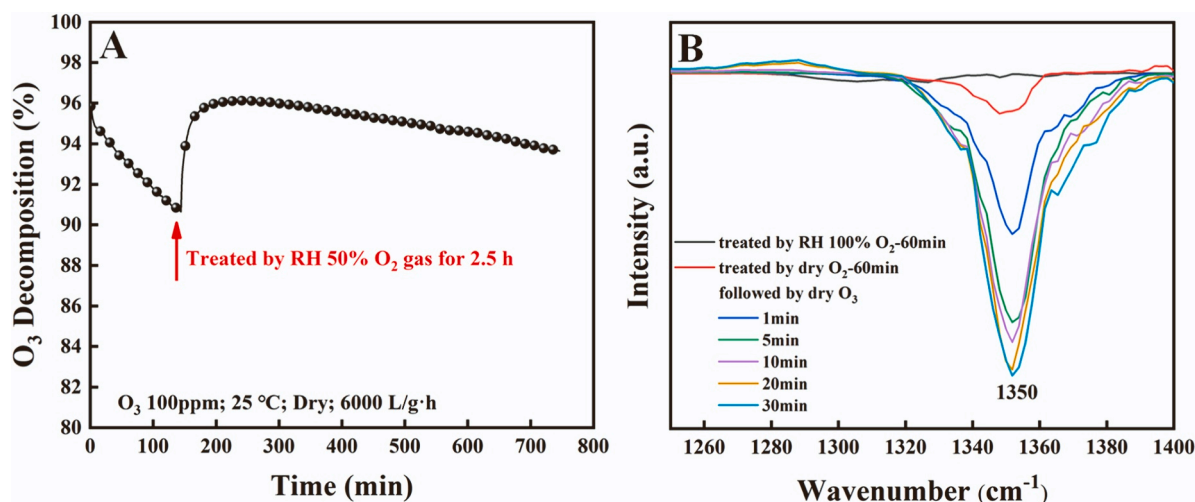

Fig. 5. (A) The effect of water on $Co_{3-x}O_4$ ozone decomposition; (B) in-situ DRFIT spectra of water-treated $Co_{3-x}O_4$ under dry O_2 and O_3 flow at room temperature.
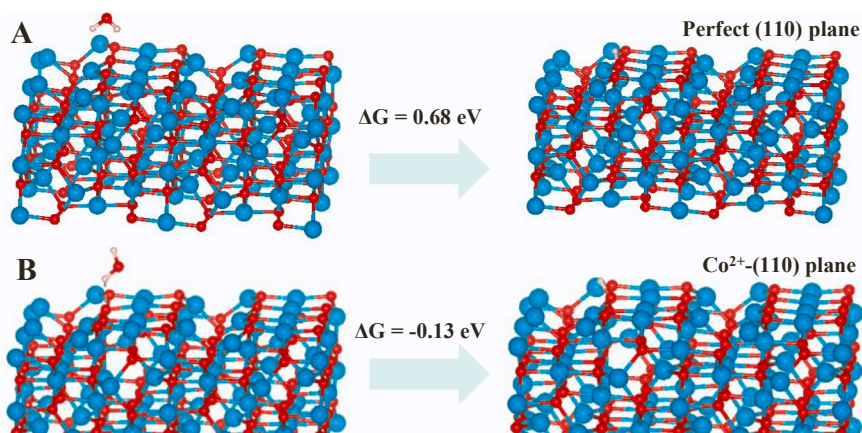
Fig. 6. Gibbs free energy of surface hydroxylation. (A) on perfect (110) plane, (B) on Co^{2+}-vacant (110) plane.

catalytic cycle of ozone decomposition over Co$_{3-x}$O$_4$. As shown in Fig. 7 A, we proposed three ozone decomposition cycles over Co$_{3-x}$O$_4$ for different conditions according to the experimental and DFT calculation results.

The first catalytic cycle (Path 1) represents the ozone decomposition under humid condition. The coordination-unsaturated oxygen first turns into OH group. And an O$_3$ molecule spontaneously adsorbed with Co^{3+} near the Co^{2+} vacancy and then bonds with OH group through hydrogen bond to form a six-membered ring, which further decomposes to release an O$_2$ molecule. After that, the second O$_3$ molecule further adsorbs on the Co^{3+} site and form a seven-membered ring in the same way, then two O$_2$ molecules desorb from the surface. The whole catalytic cycle is completed, and Co$_{3-x}$O$_4$ restores to its original state. While under dry conditions, i.e., in the absence of surface hydroxylation, ozone combines

with Co^{3+} and coordination-unsaturated oxygen to form five-membered ring, then there are two possible pathways (Path 2 and 3). Path 2 is similar to Path 1, it can complete the catalytic cycle. However, in Path 3 the coordination-unsaturated oxygen atom is consumed, resulting reduction of Co^{3+} to Co^{2+} and catalyst deactivation.

For each catalytic pathway, we calculated the reaction energy of each elementary reaction during ozone decomposition as illustrated in Fig. 7B, C, D. We can see in all three proposed catalytic cycles, the final step is the limiting step, and the first cycle has the lowest energy barrier in the final step (0.28 eV vs. 0.65 eV and 0.79 eV). Thus, the DFT calculations indicate the hydroxylation of coordination-unsaturated oxygen atom of Co^{2+}-vacant Co$_{3-x}$O$_4$ accelerates the ozone decomposition and avoid the catalyst deactivation, i.e., the OH group makes Co$_{3-x}$O$_4$ have high and stable activity for ozone decomposition.

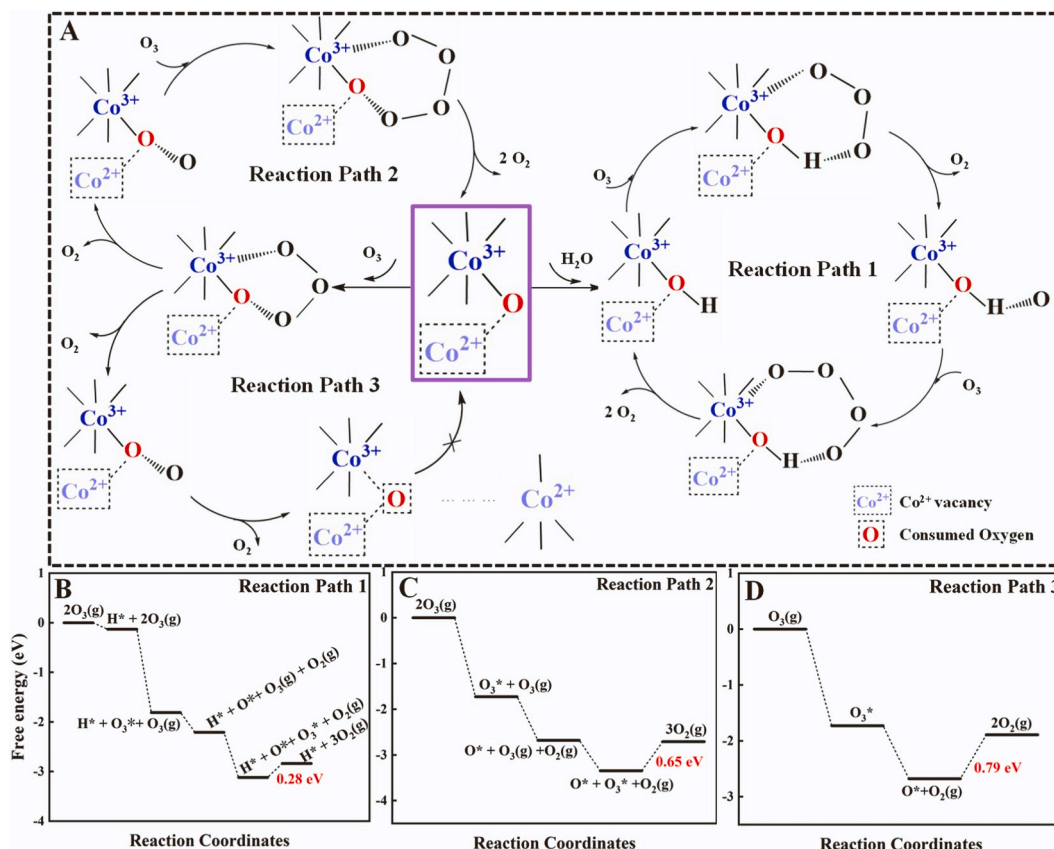**Fig. 7.** (A) Three O$_3$ decomposition pathways over Co$_{3-x}$O$_4$ under humid or dry condition; (B, C, D) Free energy diagrams of three ozone decomposition pathways.

4. Conclusions

In summary, we synthesized a Co^{2+}-vacant Co_3O_4 ($Co_{3-x}O_4$) with dominant exposure facet of (110). The existence of Co^{2+} vacancy significantly enhances the preferential adsorption of ozone over water on Co^{3+} site, accordingly greatly inhibits the adverse impact of water vapor and improve the activity of $Co_{3-x}O_4$ under humid conditions. Not only that, under humid conditions, coordination-unsaturated oxygen atoms accompanying the Co^{2+} vacancies easily become hydroxyl groups, which work together with Co^{3+} to decompose ozone and avoid the catalyst deactivation due to surface hydroxyl consumption during ozone decomposition. As a result, as-synthesized $Co_{3-x}O_4$ exhibits high activity and excellent stability even under RH as high as 90%, as well as under ultrahigh WHSV of 6000 L/g·h.

CRediT authorship contribution statement

Huinan Li: Experiment design, Methodology, Data acquisition and curation, Investigation, Writing – original manuscript. **Pengyi Zhang:** Supervision, Project administration, Funding acquisition, manuscript writing and editing. **Jingbo Jia** and **Xianjie Wang:** Supervision and editing. **Shaopeng Rong:** DFT calculations.

All authors have read and agreed to the published version of this manuscript.

Declaration of Competing Interest

The authors declare that they have no known competing financial interests or personal relationships that could have appeared to influence the work reported in this paper.

Data availability

Data will be made available on request.

Appendix A. Supporting information

Supplementary data associated with this article can be found in the online version at doi:10.1016/j.apcatb.2023.123222.

References

[1] Environmental Protection Agency U.S, Ground-level ozone pollution. ⟨https://www.epa.gov/ground-level-ozone-pollution/ground-level-ozone-basics⟩, 2019 (accessed 5 May 2023).

[2] C. Cai, J. Avise, A. Kaduwela, J. DaMassa, C. Warneke, J.B. Gilman, W. Kuster, J. de Gouw, R. Volkamer, P. Stevens, B. Lefer, J.S. Holloway, I.B. Pollack, T. Ryerson, E. Atlas, D. Blake, B. Rappenglueck, S.S. Brown, W.P. Dube, Simulating the weekly cycle of NOx-VOC-HOx-O$_3$ photochemical system in the south coast of California during CalNex-2010 campaign, J. Geophys. Res. Atmos. 124 (2019) 3532–3555.

[3] C.J. Weschler, Ozone in indoor environments: concentration and chemistry, Indoor Air 10 (2000) 269–288.

[4] T. Tao, Y. Shi, K.M. Gilbert, X. Liu, Spatiotemporal variations of air pollutants based on ground observation and emission sources over 19 Chinese urban agglomerations during 2015-2019, Sci. Rep. 12 (2022) 4293.

[5] J.L. Crooks, R. Licker, A.L. Hollis, B. Ekwurzel, The ozone climate penalty, NAAQS attainment, and health equity along the Colorado Front Range, J. Expo. Sci. Environ. Epidemiol. 32 (2022) 545–553.

[6] G. Yang, Y. Liu, X. Li, Spatiotemporal distribution of ground-level ozone in China at a city level, Sci. Rep. 10 (2020) 7229..

[7] S. Magzamen, B.F. Moore, M.G. Yost, R.A. Fenske, C.J. Karr, Ozone-related respiratory morbidity in a low-pollution region, Occup. Environ. Med 59 (2017) 624–630.

[8] H. Li, S. Wu, L. Pan, J. Xu, J. Shan, X. Yang, W. Dong, F. Deng, Y. Chen, M. Shima, X. Guo, Short-term effects of various ozone metrics on cardiopulmonary function in chronic obstructive pulmonary disease patients: Results from a panel study in Beijing, China, Environ. Pollut. 232 (2018) 358–366.

[9] A. Juginovic, M. Vukovic, I. Aranza, V. Bilos, Health impacts of air pollution exposure from 1990 to 2019 in 43 European countries, Sci. Rep. 11 (2021) 22516.

[10] D. Srivastava, T.V. Vu, S. Tong, Z. Shi, R.M. Harrison, Formation of secondary organic aerosols from anthropogenic precursors in laboratory studies, npj Clim. Atmos. Sci. 5 (2022) 22.

[11] L. Li, P. Zhang, R. Cao, Porous manganese oxides synthesized with natural products at room temperature: a superior humidity-tolerant catalyst for ozone decomposition, Catal. Sci. Technol. 10 (2020) 2254–2267.

[12] X. Liang, L. Wang, T. Wen, H. Liu, J. Zhang, Z. Liu, C. Zhu, C. Long, Mesoporous poorly crystalline α-Fe$_2$O$_3$ with abundant oxygen vacancies and acid sites for ozone decomposition, Sci. Total Environ. 804 (2022), 150161.

[13] X. Shao, X. Li, J. Ma, R. Zhang, H. He, Terminal hydroxyl groups on Al$_2$O$_3$ supports influence the valence state and dispersity of Ag nanoparticles: implications for ozone decomposition, ACS Omega 6 (2021) 10715–10722.

[14] Z. Wang, Y. Chen, X. Li, G. He, J. Ma, H. He, Layered double hydroxide catalysts for ozone decomposition: the synergic role of M^{2+} and M^{3+}, Environ. Sci. Technol. 56 (2022) 1386–1394.

[15] Z. Sun, Y. Si, S. Zhao, Q. Wang, S. Zang, Ozone decomposition by a manganese-organic framework over the entire humidity range, J. Am. Chem. Soc. 143 (2021) 5150–5157.

[16] B. Dhandapani, S.T. Oyama, Gas phase ozone decomposition catalysts, Appl. Catal. B 11 (1997) 129–166.

[17] Q. Yu, H. Pan, M. Zhao, Z. Liu, J. Wang, Y. Chen, M. Gong, Influence of calcination temperature on the performance of Pd-Mn/SiO$_2$-Al$_2$O$_3$ catalysts for ozone decomposition, J. Hazard. Mater. 172 (2009) 631–634.

[18] P. Zhang, B. Zhang, R. Shi, Catalytic decomposition of low level ozone with gold nanoparticles supported on activated carbon, Front. Environ. Sci. Eng. 3 (2009) 281–288.

[19] X. Li, J. Ma, H. He, Recent advances in catalytic decomposition of ozone, J. Environ. Sci. 94 (2020) 14–31.

[20] R. Cao, L. Li, P. Zhang, L. Gao, S. Rong, Regulating oxygen vacancies in ultrathin δ-MnO$_2$ nanosheets with superior activity for gaseous ozone decomposition, Environ. Sci. Nano 8 (2021) 1628–1641.

[21] M. Stoyanova, P. Konova, P. Nikolov, A. Naydenov, S. Christoskova, D. Mehandjiev, Alumina-supported nickel oxide for ozone decomposition and catalytic ozonation of CO and VOCs, Chem. Eng. J. 122 (2006) 41–46.

[22] T. Mathew, K. Suzuki, Y. Ikuta, Y. Nagai, N. Takahashi, H. Shinjoh, Mesoporous ferrihydrite-based iron oxide nanoparticles as highly promising materials for ozone removal, Angew. Chem. Int. Ed. 50 (2011) 7381–7384.

[23] S. Gong, A. Wang, J. Zhang, J. Guan, N. Han, Y. Chen, Gram-scale synthesis of ultra-fine Cu$_2$O for highly efficient ozone decomposition, RSC Adv. 10 (2020) 5212–5219.

[24] W. Tang, H. Liu, X. Wu, Y. Chen, Higher oxidation state responsible for ozone decomposition at room temperature over manganese and cobalt oxides: effect of calcination temperature, Ozone Sci. Eng. 36 (2014) 502–512.

[25] G. Zhu, J. Zhu, W. Li, W. Yao, R. Zong, Y. Zhu, Q. Zhang, Tuning the K$^+$ concentration in the tunnels of α-MnO$_2$ to increase the content of oxygen vacancy for ozone elimination, Environ. Sci. Technol. 52 (2018) 8684–8692.

[26] S. Gong, X. Wu, J. Zhang, N. Han, Y. Chen, Facile solution synthesis of Cu$_2$O–CuO–Cu(OH)$_2$ hierarchical nanostructures for effective catalytic ozone decomposition, CrystEngComm 20 (2018) 3096–3104.

[27] W. Li, G.V. Gibbs, S.T. Oyama, Mechanism of ozone decomposition on a manganese oxide catalyst. 1. In situ Raman spectroscopy and Ab initio molecular orbital calculations, J. Am. Chem. Soc. 120 (1998) 9041–9046.

[28] G. Zhu, W. Zhu, Y. Lou, J. Ma, W. Yao, R. Zong, Y. Zhu, Encapsulate alpha-MnO$_2$ nanofiber within graphene layer to tune surface electronic structure for efficient ozone decomposition, Nat. Commun. 12 (2021) 4152.

[29] Y. Yang, P. Zhang, J. Jia, Vanadium-doped MnO$_2$ for efficient room-temperature catalytic decomposition of ozone in air, Appl. Surf. Sci. 484 (2019) 45–53.

[30] Z. Xu, W. Yang, W. Si, J. Chen, Y. Peng, J. Li, A novel gamma-like MnO$_2$ catalyst for ozone decomposition in high humidity conditions, J. Hazard. Mater. 420 (2021), 126641.

[31] W. Hong, T. Zhu, Y. Sun, H. Wang, X. Li, F. Shen, Enhancing oxygen vcancies by introducing Na$^+$ into OMS-2 tunnels to promote catalytic ozone decomposition, Environ. Sci. Technol. 53 (2019) 13332–13343.

[32] J. Qiu, W. Zhang, J. Wang, M. Zhao, Y. Chen, Efficient monolithic MnOx catalyst prepared by heat treatment for ozone decomposition, Environ. Sci. Pollut. Res. 29 (2022) 44324–44334.

[33] D. Yan, Y. Li, J. Huo, R. Chen, L. Dai, S. Wang, Defect chemistry of nonprecious-metal electrocatalysts for oxygen reactions, Adv. Mater. 29 (2017), 1606459.

[34] C. Xie, et al., Insight into the design of defect electrocatalysts: from electronic structure to adsorption energy, Mater. Today 31 (2019) 47–68.

[35] D. Larcher, G. Sudant, R. Patrice, J.M. Tarascon, Some insights on the use of polyols-based metal alkoxides powders as precursors for tailored metal-oxides particles, Chem. Mater. 15 (2003) 3543–3551.

[36] R. Zhang, Y. Zhang, L. Pan, G. Shen, N. Mahmood, Y. Ma, Y. Shi, W. Jia, L. Wang, X. Zhang, W. Xu, J. Zou, Engineering cobalt defects in cobalt oxide for highly efficient electrocatalytic oxygen evolution, ACS Catal. 8 (2018) 3803–3811.

[37] X. Xie, Y. Li, Z. Liu, M. Haruta, W. Shen, Low-temperature oxidation of CO catalysed by Co_3O_4 nanorods, Nature 458 (2009) 746–749.

[38] G. Zhou, K. Gou, G. Li, Diffraction of crystals and quasicrystals, Peking University Press, Beijing, 2013.

[39] L. Pan, S. Wang, W. Mi, J. Song, J. Zou, L. Wang, X. Zhang, Undoped ZnO abundant with metal vacancies, Nano Energy 9 (2014) 71–79.

[40] S. Wang, L. Pan, J. Song, W. Mi, J. Zou, L. Wang, Titanium-defected undoped anatase TiO_2 with p-type conductivity, room-temperature ferromagnetism, and remarkable photocatalytic performance, J. Am. Chem. Soc. 137 (2015) 2975–2983.

[41] X. Wan, L. Wang, S. Zhang, H. Shi, J. Niu, G. Wang, W. Li, D. Chen, H. Zhang, X. Zhou, W. Wang, Ozone decomposition below room temperature using Mn-based mullite YMn_2O_5, Environ. Sci. Technol. 56 (2022) 8746–8755.

[42] M. Stoyanova, P. Konova, P. Nikolov, A. Naydenov St., D. Christoskova, Mehandjiev, Alumina-supported nickel oxide for ozone decomposition and catalytic ozonation of CO and VOCs, Chem. Eng. J. 122 (2006) 41–46.

[43] Y. Yang, D. Shen, P. Zhang, The effect of heat treatment in different atmospheres on tungsten-doped MnO_2 for ozone decomposition, Ozone Sci. Eng. 43 (2020) 195–206.